MRS Advances
https://doi.org/10.1557/s43580-026-01608-5

ORIGINAL PAPER

Electron backscatter diffraction characterisation of a zirconolite-rich multi-phase ceramic wasteform

Pranesh Dayal[1] · **Ondrej Muransky**[1] · **Thanh Ha Nguyen**[1] · **Daniel J. Gregg**[1]

Received: 23 December 2025 / Accepted: 27 February 2026

Abstract

Single- or multi-phase ceramics and glass–ceramic composite materials are widely recognised as candidate wasteforms for the immobilisation of intermediate- and high-level radioactive wastes (ILW and HLWs). The long-term performance of these materials is governed by their microstructural features which may include grain size, crystallographic orientation, and phase distribution. These attributes influence dissolution rates, material response to radiation damage, and mechanical integrity, making them essential parameters in predictive models of wasteform durability over extended timescales. However, quantitative determination of grain-size and phase composition in ceramic and glass–ceramic wasteforms remains scarcely reported due to the inherent limitations of conventional methods. Here we present a novel methodology to produce reliable Electron Backscatter Diffraction (EBSD) maps of complex multi-phase systems to address this challenge. The approach enables precise grain-size measurement, phase quantification, texture analysis, and interphase boundary characterisation, in single- and multi-phase ceramics and glass–ceramic materials, significantly advancing microstructural assessment in nuclear wasteform research.

Introduction

Radioactive waste is generated from a broad range of activities, including civilian programmes such as nuclear power, used nuclear fuel reprocessing and nuclear medicine generation, as well as military applications such as legacy nuclear weapons production and submarine propulsion. The safe management of this waste is essential to protect both the environment and future generations, and it is a prerequisite for sustaining the continued growth of nuclear technologies. Several candidate wasteforms have been proposed for the long-term immobilisation of intermediate- and high-level radioactive wastes (ILW and HLWs), ranging from glass [1] to glass–ceramic composites [2, 3] and single- and multi-phase ceramic systems [4], each at different stages of research and development and deployment. Ultimately, all wasteforms for ILW and HLW are intended for disposal in nuclear waste repositories. However, before such disposal can be implemented, it is critical to understand how these materials will interact with their surrounding environment over timescales of up to hundreds of thousands of years [5]. The majority of studies reported in the literature focus on the performance of these wasteforms in aqueous environments [6–10], typically employing short-term standardised dissolution tests. This focus reflects the expectation that during their disposal in the waste repository, the wasteform will eventually come into contact with groundwater.

Grain boundaries are known to influence the dissolution rate of ceramic materials in aqueous environments through preferential dissolution [11, 12]. This implies that ceramic wasteforms with finer grains, and therefore a higher fraction of grain boundaries, may exhibit higher dissolution rates. Conversely, wasteform materials typically target smaller grain sizes to minimise radiation damage impacts, as grain boundaries act as barriers to the propagation of radiation damage [13, 14]. The mechanical properties of ceramic wasteforms also depend on grain size [15]. Therefore, achieving an optimal grain-size distribution is essential to maximise the performance of ceramic and glass–ceramic wasteforms.

In multi-phase systems, each phase may have its own corrosion rate [16, 17]. Consequently, an accurate assessment of aqueous durability requires quantitative determination of phase abundances in the multi-phase ceramic or

✉ Pranesh Dayal
praneshd@ansto.gov.au

[1] Australian Nuclear Science and Technology Organisation, Locked Bag 2001, Kirrawee DC, Lucas Heights, NSW 2232, Australia

Published online: 19 March 2026

glass–ceramic. Aqueous durability may also be influenced by crystallographic orientation, and in multi-phase systems different types of interphase boundaries may behave differently, although studies exploring this hypothesis remain scarce in the literature. Despite their importance, grain-size measurements in nuclear wasteform research also remain limited. Traditional methods such as chemical [18] or thermal [18] etching followed by grain-size analysis often fail in multi-phase ceramic samples, where individual phases cannot be reliably distinguished [19]. Moreover, during thermal etching, elevated temperature and sufficient time can cause smaller grains to be absorbed by larger ones, leading to grain growth and a resulting change in the microstructure [18]. However, accurately determining and collectively assessing the wasteform microstructural features provide important information when evaluating the long-term performance of ceramic and glass–ceramic wasteforms, and their integration, therefore, into durability models helps ensure reliable long-term predictions.

Electron Backscatter Diffraction (EBSD) is a well-established and effective technique for grain analysis and has been used extensively for metals [20]. However, applying EBSD to ceramics present challenges such as charging, drift, and the optimisation of coating thickness [21], and most significantly, difficulties in obtaining accurate crystallographic information files (CIF). Without correct CIF files, EBSD maps are of poor quality regardless of the quality of the electron backscatter patterns, as the software fails to index the phases properly. This issue becomes increasingly complex when wasteform samples are doped with actinides or surrogate elements.

Here, we present a methodological approach to address this issue for a multi-phase Synroc-type ceramic targeting zirconolite, hollandite and rutile ceramic phases. We describe a detailed method for generating CIF files for each phase in a multi-phase system based on X-ray diffraction (XRD) data, and we demonstrate how these CIF files can be used to produce high-quality EBSD maps. Using this approach, we determine grain-size distributions, crystallographic texture, quantitative phase abundances, qualitative phase distributions, and interphase boundary characteristics.

Materials and methods

Sample preparation

A zirconolite-rich multi-phase ceramic was synthesised using hot isostatic pressing (HIPing) targeting ~ 80 wt.% zirconolite (nominally $Ca_{0.595}Ce_{0.27}Gd_{0.135}Sm_{0.135}Hf_{0.27}Zr_{0.595}Ti_{1.73}Al_{0.27}O_7$) and ~ 10 wt.% each of Ba-hollandite (nominally $BaAl_2Ti_6O_{16}$) and rutile (nominally TiO_2). The composition was based on a zirconolite-rich multi-phase ceramic designed during the United States Plutonium Immobilisation Project (US PIP programme) and using Ce as an analogue for Pu [4, 22–24]. The sample was prepared (50 g) using an alkoxide-nitrate route, in which Ce was introduced as a nitrate solution prior to calcination at 700 °C in argon for 1 h. The calcined powder was then ball milled, dried, and loaded into a stainless-steel HIP canister. The HIP canister was evacuated and sealed and HIPed using an IPS Eagle HIP at 1280 °C for 3 h under a pressure of 150 MPa.

Energy-dispersive X-ray spectroscopy (EDS)

The HIPed canister was sectioned, and a sample was extracted from its centre. The sample was then mounted in epoxy resin and polished to a 1 µm diamond finish, followed by a final polishing step using an MD-Chem cloth. This final step was performed to obtain a sample surface with minimal deformation, suitable for EBSD mapping, since diffracted electrons are generated from a surface layer on the order of a few tens of nanometres thick. The sample was coated with ~ 2 nm of carbon to avoid charging effects. The wasteform material was examined using a Zeiss Ultra Plus scanning electron microscope (SEM) (Carl Zeiss NTS GmbH, Oberkochen, Germany) operating at 15 kV accelerating voltage and equipped with an Ultim® Max 170 mm^2 SDD energy-dispersive X-ray spectroscopy (EDS) system (Oxford Instruments, Abingdon, Oxfordshire, UK). Measurements were conducted using an aperture of 60 µm and a working distance of 10 mm.

Energy-dispersive X-ray spectra were acquired in *Auto Acquisition Mode*, in which data were collected until sufficient counts were obtained for the software to perform quantification. EDS measurements were taken at a minimum of five locations per phase.

X-ray diffraction (XRD) analysis

XRD measurements were performed using a Bruker D8 Advance diffractometer equipped with a Cu Kα radiation source ($\lambda = 1.5418$ Å) and a Ni filter (0.02), fitted with a Lynxeye XE detector. Data were collected over the range $5° \leq 2\theta \leq 90°$ with a step size of 0.02°, spinning speed of 15 rpm and a counting time of 2 s per step.

The diffraction data were indexed using Bruker EVA software with reference to the PDF-2 + database and CIF files obtained from the ICSD database. Only unit cell parameters were refined using the Rietveld method implemented in TOPAS v5 software. A new CIF file containing the refined cell parameters was generated for each phase and subsequently used for EBSD analysis. A more detailed refinement, incorporating additional parameters, could further improve the CIF file and potentially the resulting EBSD quality.

Electron backscatter diffraction (EBSD)

The grain structure and phase composition were characterised using a Zeiss Ultra Plus SEM (Carl Zeiss NTS GmbH, Oberkochen, Germany) operating at 20 kV accelerating voltage and equipped with a Symmetry electron backscatter diffraction (EBSD) detector (Oxford Instruments, Abingdon, Oxfordshire, UK). Measurements were conducted using a 120 µm aperture, a working distance of 15 mm, and a tilt angle of 70°. The step size used to acquire the EBSD map was 20 nm.

EBSD pattern indexing was performed using a refined-accuracy solver with detection of ten Kikuchi bands per pattern and a Hough transform resolution of 40. Solution refinement was enabled to improve pattern matching accuracy. Phase discrimination was assisted by simultaneous energy-dispersive X-ray spectroscopy (EDS), using an energy range up to 20 keV with 2048 channels and pulse pile-up correction enabled.

Low-quality or poorly indexed points were excluded based on pattern quality and confidence metrics provided by the acquisition software. Post-acquisition processing was carried out using the MTEX MATLAB toolbox. Isolated mis-indexed pixels were removed using a neighbour consensus smoothing algorithm considering up to third-order neighbouring points, and additional orientation noise was reduced using a half-quadratic variational smoothing filter. Grain reconstruction was performed using misorientation thresholds of 1° for low-angle boundaries and 5° for high-angle boundaries. Grains smaller than 50 pixels and highly elongated artefacts were removed prior to quantitative analysis, and remaining non-indexed pixels were filled and extrapolated based on neighbouring grain orientations.

Results and discussion

SEM micrographs revealed a completely dense sample and uniform microstructure with zirconolite as the predominant phase. No bright regions indicative of unreacted CeO_2 were observed in the SEM micrographs, confirming complete incorporation of cerium, a surrogate for actinides, within the host zirconolite phase. The SEM–EDS-measured chemical compositions of the three phases, along with their comparison to the corresponding designed compositions, are presented in Table 1. The measured zirconolite composition (assuming a total of four cations on the Ca-, Zr-, and Ti sites) closely matched the target formulation, although slightly lower amounts of Ce and Zr were observed in the measured composition. This deficit appeared to be compensated by increased incorporation of Al. The presence of Ca, Ce, Sm, Gd, Zr and Hf in hollandite grain analyses was indicative of elemental contributions from nearby zirconolite grains. The average zirconolite composition was therefore scaled and removed from the average measured composition of hollandite grains such that Zr was eliminated to provide a "deduced" hollandite composition. The deduced elemental composition of hollandite is presented in Tabel 1 assuming a total of 8 cations on the Al- and Ti-sites. The data showed slightly increased Al incorporation relative to the target formulation and correspondingly reduced Ti content. Analysis of rutile grains indicated the incorporation of minor amounts Zr, Hf, Al and Ca, though contributions from adjacent zirconolite grains cannot be discounted.

The XRD pattern from material extracted from the HIP canister confirmed the targeted zirconolite, hollandite, and rutile phase formation (Fig. 1) and results from data refinement are summarised in Table 2. The unit cell parameters associated with the CIF files obtained from the ICSD database for the zirconolite 3T (ICSD #97419), hollandite (ICSD #60863), and rutile (ICSD #33838) phases are summarised in the second column of Table 2 as the original CIF values. These unit cell parameters were then refined using the Rietveld method to match the XRD data collected for the Ce-doped, zirconolite-rich wasteform material, and the refined values are reported in the third column of Table 2. Using these refined parameters, a new EBSD-software-compatible CIF file was generated for each phase and subsequently used for EBSD mapping.

The microstructural architecture and interfacial characteristics of the ceramic wasteform were quantified using EBSD mapping. As shown in Fig. 2a–b, the specimen exhibits a dense, fine-grained microstructure comprising three distinct phases of zirconolite (Z), rutile (R), and hollandite (H). Phase-fraction analysis confirmed zirconolite as the dominant phase (79 area %), with homogeneously distributed rutile (13 area %) and hollandite (8 area %) grains. Phase abundance was directly

Table 1 Target compositions and SEM–EDS-measured compositions of the three phases

Phase	Composition[1]
Zirconolite- Target	$Ca_{0.595}Ce_{0.270}Gd_{0.135}Sm_{0.135}Hf_{0.270}Zr_{0.595}Ti_{1.730}Al_{0.270}O_7$
Zirconolite- Measured	$Ca_{0.50}Ce_{0.22}Gd_{0.13}Sm_{0.13}Hf_{0.28}Zr_{0.49}Ti_{1.74}Al_{0.40}O_7$
Rutile- Target	TiO_2
Rutile- Measured	$Ti_{0.74}Zr_{0.06}Hf_{0.04}Al_{0.04}Ca_{0.05}O_2$
Hollandite- Target	$BaAl_2Ti_6O_{16}$
Hollandite- Deduced	$Ba_{1.22}Al_{2.25}Ti_{5.75}O_{16}$

[1]Major elements provided. Due to the fine-grained structure of the material, hollandite analyses exhibited contributions from adjacent zirconolite grains, presenting challenges in isolating pure phase compositions. The number of moles of oxygen is assumed for each individual phase

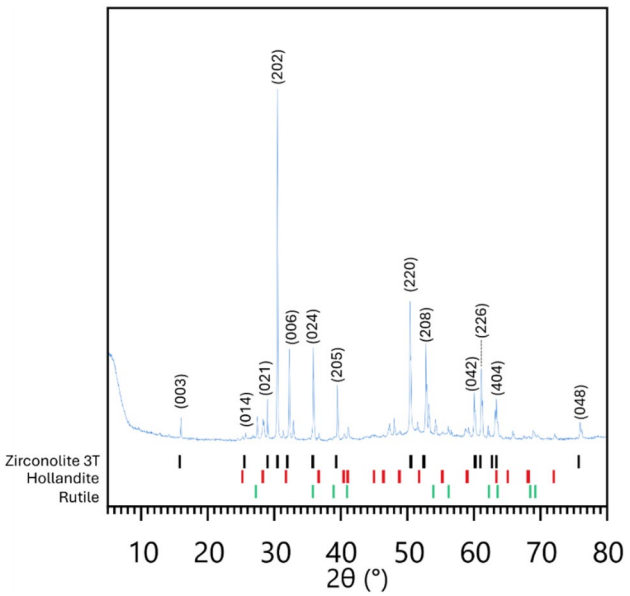

Fig. 1 X-ray diffraction pattern from material extracted from the HIP canister. Miller indices are for the zirconolite 3T phase. Tick marks show allowed reflections with $I > 5\%\ I_{Max}$

converted from an area percentage for the two-dimensional slice to vol.%, assuming equiaxed grains. This translates to approximately 80 wt.% zirconolite, 8 wt.% hollandite, and 12 wt.% rutile assuming 4.8, 4.7, and 4.2 g/cm^3 for zirconolite, hollandite, and rutile densities, respectively (noting the large error expected for the density values due to the range of chemistries incorporated in each of the phases). The measured wt.% composition values closely match the targeted values.

The Z-direction inverse pole figure (IPF) in Fig. 2c indicates no clear preferential crystallographic orientation across the mapped area, consistent with a near-random texture for all constituent phases. Quantitative grain-morphology analysis (boxplots in Fig. 2d) reveals a sub-micron microstructure for each phase. Zirconolite shows the broadest size distribution with a mean equivalent diameter of 0.63 ± 0.28 µm, whilst the secondary phases are marginally finer with mean equivalent diameters of 0.53 ± 0.20 µm and 0.43 ± 0.16 µm for rutile and hollandite, respectively (noting that edge grains were excluded from the grain-size measurements, as shown in Fig. 2b).

Crystallographic relationships between grains were assessed via boundary misorientation analysis (Fig. 2e). Homo-phase boundaries generally exhibit higher misorientation angles than hetero-phase interfaces. Notably, hollandite-hollandite (H–H) boundaries present the highest mean misorientation (88.9°),

Table 2 Refined lattice parameters and cell volumes for the phases present

Parameter	Original CIF value	Rietveld-refined value
Zirconolite 3T (ICSD #97419)		
Crystal system	Trigonal	Trigonal
Space group	P3121 (152)	P3121 (152)
a/b	7.228(1)	7.239(2)
c	16.805(1)	16.649(5)
Alpha/Beta	90.0000	90.0000
Gamma	120.0000	120.0000
Cell volume	760.34	755.6(5)
Hollandite (ICSD #60863)		
Crystal system	Tetragonal	Tetragonal
Space group	I4/m (87)	I4/m (87)
a/b	9.9750(1)	9.964(4)
c	2.92538(4)	2.925(3)
Alpha/Beta	90.0000	90.0000
Gamma	90.0000	90.0000
Cell volume	291.08	290.4(4)
Rutile (ICSD #33838)		
Crystal system	Tetragonal	Tetragonal
Space group	P42/mnm (136)	P42/mnm (136)
a/b	4.6001(3)	4.5985(9)
c	2.9654(4)	2.9709(11)
Alpha/Beta	90.0000	90.0000
Gamma	90.0000	90.0000
Cell volume	62.75	62.82(3)

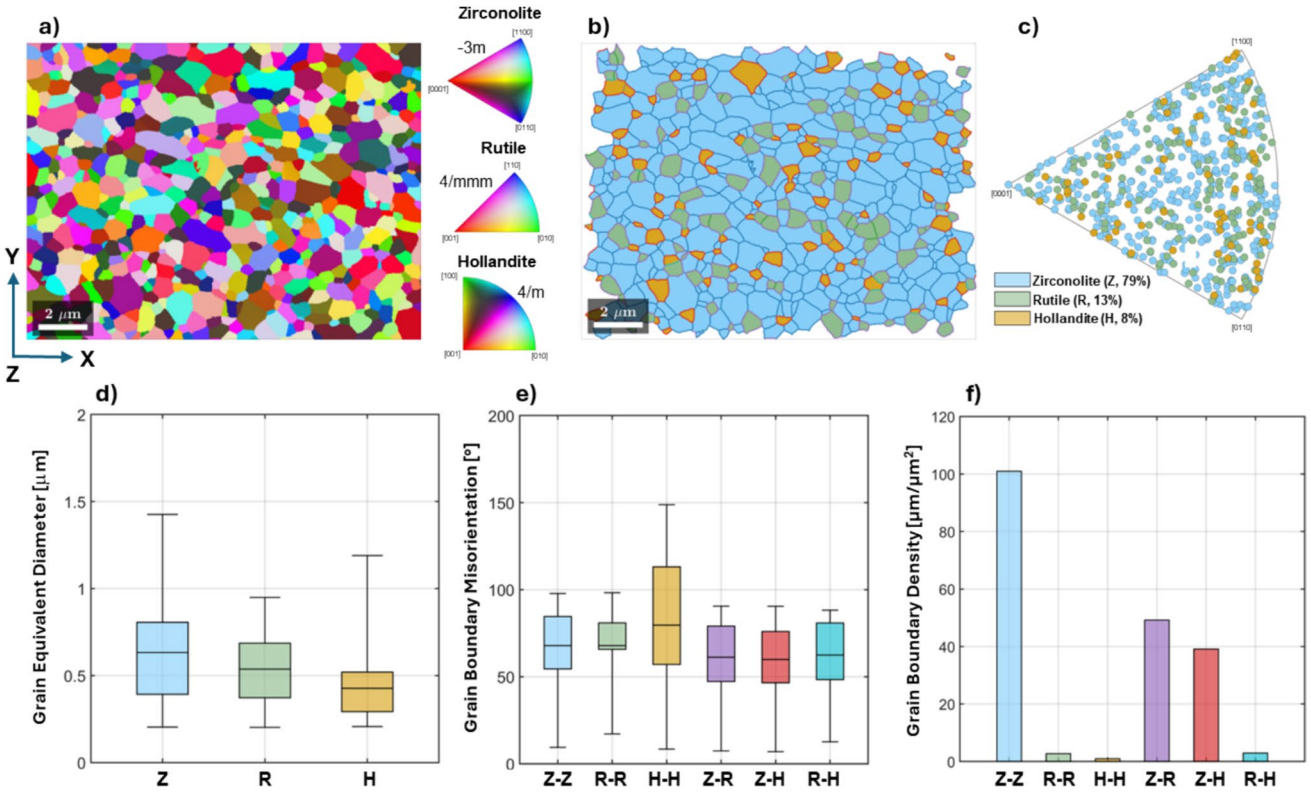

Fig. 2 **a** EBSD orientation map presented as an Inverse Pole Figure (IPF), Z direction, showing the crystallographic orientation of individual grains. **b** Phase distribution map identifying zirconolite (Z, blue, 79 area %), rutile (R, green, 13 area %), and hollandite (H, orange, 8 area %) grains, overlaid with reconstructed grain boundaries; edge grains were excluded from the grain-size and grain-boundary analyses. **c** IPF in Z direction summarising the mean grain orientations for each identified constituent phase. **d** Boxplot statistics of grain-size distributions expressed as equivalent diameters for all three identified phases. **e** Misorientation-angle distributions for homo-phase (Z–Z, R–R, H–H) and hetero-phase (Z–R, Z–H, R–H) boundaries. **f** Bar chart quantifying grain-boundary density (μm/μm^2) for the same interface types

significantly exceeding that of Z-Z (68.2°) and R-R (67.4°) boundaries. The hetero-phase interfaces (Z-R, Z-H, and R-H) cluster within a lower mean misorientation range of 60° to 62°.

The connectivity of the phases was further evaluated through grain boundary density calculations (Fig. 2f). The microstructure is dominated by Z-Z boundaries (108.4 μm/μm^2), consistent with the high area fraction (79 area %) and continuity of the zirconolite matrix. Significant densities for Z-R (52.4 μm/μm^2) and Z-H (41.5 μm/μm^2) interfaces indicate extensive wetting of the secondary phases by the zirconolite matrix. Conversely, the negligible densities recorded for R-R (2.9 μm/μm^2), R-H (3.2 μm/μm^2), and H–H (0.8 μm/μm^2) boundaries confirm that the dispersed rutile and hollandite grains remain largely isolated from one another.

Conclusions

The combined SEM–EDS, XRD, and SEM-EBSD analyses demonstrated that the Ce-doped, zirconolite-rich HIPed multi-phase ceramic successfully achieved the intended phase assemblage and phase elemental compositions. Crystallographic parameters were refined through integration of ICSD reference structures with experimentally measured XRD data, facilitating the generation of phase-accurate CIF files suitable for advanced EBSD structural analysis.

EBSD mapping revealed a dense, fine-grained, predominantly zirconolite matrix containing well-distributed rutile and hollandite secondary phases. All phases exhibited near-random crystallographic textures and sub-micron grain sizes, with zirconolite exhibiting the broadest size distribution. Grain boundary misorientation analysis indicated that hollandite–hollandite (H–H) boundaries display higher mean misorientation angles than other homo-phase and hetero-phase interfaces, reflecting distinct crystallographic variability within this phase. Grain-boundary density metrics further highlighted the predominant interconnectivity of the zirconolite matrix, which extensively wets the adjacent secondary phases. Conversely, rutile and hollandite grains exhibit minimal mutual interaction, remaining largely isolated due to their low mutual boundary densities.

This study established a robust EBSD-based methodology for quantitative microstructural characterisation of multi-phase ceramic wasteforms, overcoming the limitations of conventional techniques. The approach enables quantitative determination of grain-scale features including phase distribution, homo- and hetero-phase interfaces, boundary connectivity, and crystallographic variability. These attributes can be included into refined predictive models of long-term multi-phase ceramic wasteform performance.

Acknowledgments The authors would like to acknowledge ANSTO staff present and previous for sample formulation and synthesis, including Neil Webb for HIP support. We would also like to thank Bruce Begg, Zhiyang Wang, Daniel Bailey and Colleen Mann for helpful discussions, and Annastasia Bedford for metallographic specimen preparation.

Author's contributions Pranesh Dayal: Conceptualization, EDS—experimental and data analysis, EBSD—experimental and data analysis, writing–original draft. Ondrej Muransky: Conceptualization, EBSD—data analysis, writing—EBSD analysis. Thanh Ha Nguyen: Conceptualization, XRD—experimental and data analysis, writing—XRD analysis. Daniel J. Gregg: Conceptualization, EDS—data analysis, writing—review and editing.

Funding Open Access funding enabled and organized by CAUL and its Member Institutions. Not applicable.

Data availability Data will be made available on request.

Declarations

Conflict of Interest The authors declare no conflict of interest.

References

1. N.R. Council, *Waste Forms Technology and Performance: Final Report*. Washington, DC: The National Academies Press (2011)
2. J.S. McCloy, A. Goel, Glass-ceramics for nuclear-waste immobilization. MRS Bull. **42**(3), 233–240 (2017)
3. Y. Zhang et al., Current advances on titanate glass-ceramic composite materials as waste forms for actinide immobilization: a technical review. J. Eur. Ceram. Soc. **42**(5), 1852–1876 (2022)
4. D.J. Gregg et al., Synroc technology: perspectives and current status (review). J. Am. Ceram. Soc. **103**(10), 5424–5441 (2020)
5. G.S. Frankel et al., Recent advances in corrosion science applicable to disposal of high-level nuclear waste. Chem. Rev. **121**(20), 12327–12383 (2021)
6. G.S. Frankel et al., A comparative review of the aqueous corrosion of glasses, crystalline ceramics, and metals. npj. Mater. Degrad. **2**(1), 15 (2018)
7. Y. Zhang et al., Zirconolite-rich titanate ceramics for immobilisation of actinides – waste form/HIP can interactions and chemical durability. J. Nucl. Mater. **395**(1), 69–74 (2009)
8. K.L. Smith et al., Dissolution of synroc in deionised water at150°C. MRS Proc. **465**, 349 (1996)
9. Z. Zhang et al., Aqueous dissolution of perovskite ($CaTiO_3$): effects of surface damage and [Ca^{2+}] in the leachant. J. Mater. Res. **20**(9), 2462–2473 (2005)
10. S. Myhra et al., Hydrothermal dissolution of perovskite ($CaTiO_3$). J. Mater. Sci. **22**(9), 3217–3226 (1987)
11. D. Horlait et al., Environmental SEM monitoring of Ce1−xLnxO2−x/2 mixed-oxide microstructural evolution during dissolution. J. Mater. Chem. A **2**(15), 5193–5203 (2014)
12. C.L. Corkhill et al., Role of microstructure and surface defects on the dissolution kinetics of CeO_2, a UO_2 fuel analogue. ACS Appl. Mater. Interfaces **8**(16), 10562–10571 (2016)
13. T. Lender et al., Investigation of radiation damage in the monazite-type solid solution La1–xCexPO4. Inorg. Chem. **63**(38), 17525–17535 (2024)
14. S. Dey et al., Radiation tolerance of nanocrystalline ceramics: Insights from Yttria Stabilized Zirconia. Sci. Rep. **5**(1), 7746 (2015)
15. L. Kurpaska, J. Jagielski, Mechanical properties of irradiated Gd2Zr2O7 pyrochlores as studied by nanoindentation technique – Effect of grains and grain boundaries. Nucl. Instrum. Methods Phys. Res. B Beam Interact. Mater. Atoms **379**, 107–111 (2016)
16. S.K. Roberts, W.L. Bourcier, H.F. Shaw, Aqueous dissolution kinetics of pyrochlore, zirconolite and brannerite at 25, 50, and 75 °C. Radiochim. Acta **88**(9–11), 539–546 (2000)
17. G.R. Lumpkin et al., Geochemical behaviour of host phases for actinides and fission products in crystalline ceramic nuclear waste forms. Geol. Soc. Lond. Spec. Publ. **236**(1), 89–111 (2004)
18. R.E. Chinn, Etching. Metallogr. Microstruct. Anal. **4**(3), 240–257 (2015)
19. D.R. Cousens et al., The microstructure of synroc. MRS Proc. **11**, 309 (1981)
20. A.J. Schwartz et al., *Electron Backscatter Diffraction in Materials Science* (Springer, US, 2010)
21. A. Koblischka-Veneva, F. Mücklich, Orientation imaging microscopy applied to BaTiO3 ceramics. Cryst. Eng. **5**(3), 235–242 (2002)
22. A. Johnston, E. Vance, *Synroc for plutonium disposal* (Australian Nuclear Science and Technology Organisation, Australia, 1999)
23. P. Dayal et al., Profiling hot isostatically pressed canister–wasteform interaction for Pu-bearing zirconolite-rich wasteforms. J. Am. Ceram. Soc. **105**(8), 5359–5372 (2022)
24. E. Vance, et al., *Synroc derivatives for excess weapons plutonium.* Ceram. Trans., (1998)